PAPER

Electronic, optical and mechanical properties of SrSi$_6$N$_8$ and SrSi$_6$N$_8$O *via* first-principles

Zhifeng Huang, Fei Chen,* Jianwen Zhang, Qiang Shen and Lianmeng Zhang

The different properties of two structurally similar nitridosilicates, SrSi$_6$N$_8$ and SrSi$_6$N$_8$O, are attributed to the oxygen atom. To explore the effects of the O atom on the properties, structural, electronic, optical and mechanical properties of SrSi$_6$N$_8$, SrSi$_6$N$_8$O and O-doped SrSi$_6$N$_8$ have been simulated *via* first-principles in this work. The results indicate the Si–O–Si bond is stronger than the Si–Si bond, resulting in a more stable crystal structure of SrSi$_6$N$_8$O compared with SrSi$_6$N$_8$. The calculated bandgaps (E_g) of SrSi$_6$N$_8$ and SrSi$_6$N$_8$O are 3.10 and 3.97 eV, respectively. The lower E_g of SrSi$_6$N$_8$ originates from the Si–Si σ* bond, however, the E_g can be enlarged through introducing the O atom into the Si–Si bond. The optical properties illustrate that the refractive peaks are blue-shifted with O doping into the lattice of SrSi$_6$N$_8$. Furthermore, the elastic properties show that SrSi$_6$N$_8$ and SrSi$_6$N$_8$O are comparable to traditional mechanical ceramics such as sialons. This work not only expounds the difference between SrSi$_6$N$_8$ and SrSi$_6$N$_8$O, but also gives theoretical foundation for their potential applications as optical and mechanical materials.

1. Introduction

Nitridosilicates doped with active ions (such as Eu^{2+} and Ce^{3+}) have been widely used as phosphors in phosphor-converted light emitting diodes (pc-LEDs) in consideration of their high chemical and thermal stability in combination with low thermal quenching and high conversion efficiencies.[1–3] Compared to traditional phosphors such as orthosilicates (*e.g.* Sr$_2$SiO$_4$:Eu^{2+})[4] or alkaline earth sulfides (*e.g.* SrCa$_2$S$_4$:Eu^{2+}),[5] nitridosilicates have more diversiform crystal structures owing to their more varied crosslinking patterns.[6] In nitridosilicates, the N can connect up to four neighboring Si tetrahedral centers, causing a higher degree of lattice condensation to improve the chemical stability of nitride phosphors, preventing the hydrolysis reaction which often happens in phosphors with terminal or ionic O or S atoms over time.[7,8]

In the last few years, research into rare earth metals activating alkaline-earth-metal nitridosilicates-based phosphors has become increasingly important, such as MSi$_6$N$_8$ (M = Sr and Ba),[9,10] MSi$_7$N$_{10}$ (M = Sr, Ba),[11,12] M$_2$Si$_5$N$_8$ (M = Ca, Sr and Ba),[13–15] MSiN$_2$ (M = Sr, Ba),[16] and Ba$_5$Si$_2$N$_6$.[17] Among the available alkaline earth nitridosilicates-based phosphors, SrSi$_6$N$_8$ is very different from the others. For example, the oxidation states of Si are +III and +IV in SrSi$_6$N$_8$, and the framework contains single Si–Si bonds in N$_3$Si–SiN$_3$,[9] as seen in Fig. 1(a). Also, SrSi$_6$N$_8$:Eu^{2+} was reported to have blue

luminescent property of 450–455 nm,[18,19] while most of nitridosilicates-based phosphors emitted yellow to red wavelengths. Besides, because of the structural similarity compared with MSi$_6$N$_8$, MSi$_6$N$_8$O (M = Ca and Ba) based material has also been reported to have excellent luminescent properties. Fig. 1(b) shows the crystal structure of SrSi$_6$N$_8$O, which can be gained by inserting one O atom into the single Si–Si bond in SrSi$_6$N$_8$.[9] Although there is no experimental report of the preparation of pure SrSi$_6$N$_8$O, the compound of Sr$_2$Si$_{12-x}$Al$_x$N$_{16-x}$O$_{2+x}$:Eu^{2+} ($x \approx$ 2) has been synthesized by Z Shen.[20] Sr$_2$Si$_{12-x}$Al$_x$N$_{16-x}$O$_{2+x}$ exhibits an isotypic structure compared with SrSi$_6$N$_8$O, therefore the analogous silicon atoms are also bridged by oxygen atoms. Also, the photoluminescence properties of Eu activating CaSi$_6$N$_8$O and BaSi$_6$N$_8$O have been studied experimentally. The reported main photoluminescent peaks are at about 500 nm for BaSi$_6$N$_8$O:Eu^{2+},[21,22] 614 and 587 nm for BaSi$_6$N$_8$O:Eu^{3+},[23] and 405 nm for CaSi$_6$N$_8$O:Eu^{2+}.[24] Furthermore, some alkaline-earth-metal nitridosilicates have been reported to have excellent mechanical properties. For instance, SrSi$_7$N$_{10}$ has a yield hardness of 16.1(5) GPa,[11] and CaAlSiN$_3$ has been considered as a relatively hard materials from first-principles simulation.[25] However, even SrSi$_6$N$_8$ and SrSi$_6$N$_8$O have been investigated a lot in previous works, there is almost no paper having reported their basic characteristics such as electronic, optical and mechanical properties. In order to take full advantage of the properties of SrSi$_6$N$_8$ and SrSi$_6$N$_8$O for eventual technological applications, a better understanding of their electronic, optical and mechanical properties is required. What's more, the photoluminescence peaks of intrinsic and O-replacement defective SrSi$_6$N$_8$ have been reported by Wen Yeh *et al.* to locate at 452 and 652 nm,

State Key Lab of Advanced Technology for Materials Synthesis and Processing, Wuhan University of Technology, Wuhan 430070, China. E-mail: chenfei027@gmail.com; Fax: +86-27-87879468; Tel: +86-27-87168606
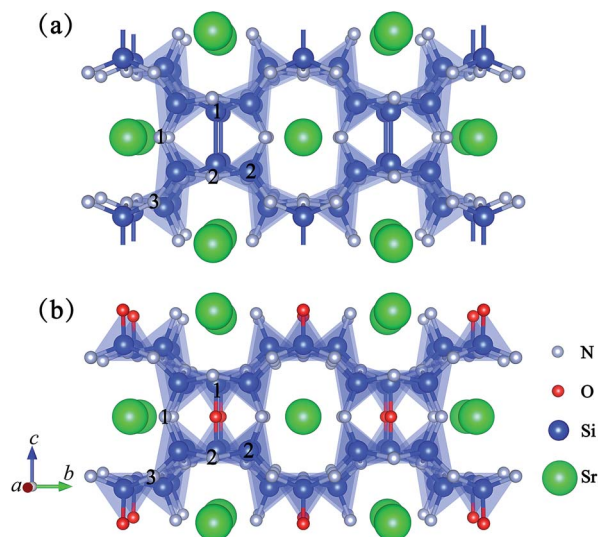
Fig. 1 Projective representation of $2 \times 2 \times 1$ supercells of (a) $SrSi_6N_8$ and (b) $SrSi_6N_8O$.

respectively.[26] The results show that the oxygen atom has significant effect on electronic and optical properties of $SrSi_6N_8$. Actually, nitrogen-rich sialon materials, with partial substitutions of Si by Al and N by O, have attracted great interest owing to their excellent optical and mechanical performance.[3] The ratio of O : N has the significant effect on the properties of sialon materials. So introducing the O atom into the lattice of $SrSi_6N_8$ may generate positive effects on electronic, optical and mechanical properties. Considering that the big difference between $SrSi_6N_8$ and $SrSi_6N_8O$ is the O atom, investigating the effect of O atom on $SrSi_6N_8$ may also give some ideas to understand the difference in their properties.

Herein, in this work, first-principles calculations[27–29] have been used to investigate the electronic, optical and mechanical properties of $SrSi_6N_8$, $SrSi_6N_8O$, and O-doped $SrSi_6N_8$. On the one hand, this work has given the comparison and explanation of the difference between $SrSi_6N_8$ and $SrSi_6N_8O$ in electronic, optical and mechanical properties. On the other hand, the effects of O atom on $SrSi_6N_8$ have also been investigated through introducing O atoms to replace different N atoms and to insert into the single Si–Si bond. This work not only explains the difference between $SrSi_6N_8$ and $SrSi_6N_8O$, but also gives the theoretical foundation for their potential applications.

2. Theoretical and computational methods

Fig. 1 shows the crystal structures of $2 \times 2 \times 1$ $SrSi_6N_8$ and $2 \times 2 \times 1$ $SrSi_6N_8O$ supercells. As seen in Fig. 1(a), there are two types of connectivity models of N atoms, which are bonded with two Si atoms (marked as $N^{[2]}$) and three Si atoms (marked as $N^{[3]}$). And the spatial locations of Si–$N^{[3]}$–Si bonds are vertical and with a certain angle to the b axis.[9] So, we marked the $N^{[2]}$ as N_1, the two N atoms in the different Si–$N^{[3]}$–Si bonds as N_2 and N_3, the Si atoms in the Si–Si bonds as Si_1, and the other Si atoms as

Si_2, as seen in Fig. 1(a). Herein, four types of O-doped $2 \times 2 \times 1$ $SrSi_6N_8$ supercells were considered in our work, which were O_i substituting to N_i ($i = 1, 2$ and 3) and O_4 inserting into the Si–Si bond, and marked as O_i–$SrSi_6N_8$ ($i = 1, 2, 3$ and 4), respectively.

All first principle calculations were performed using Cambridge Serial Total Energy Package (CASTEP) code.[29] The electronic exchange–correlation function was Perdew Burke Ernzerhof (PBE) of generalized gradient approximation (GGA).[30] Ultrasoft pseudopotentials were used with $5s^2\ 5p^0$, $3s^2\ 3p^2$, $2s^2\ 2p^3$ and $2s^2\ 2p^4$ as the valence-electron configurations for Sr, Si, N and O atoms, respectively, to describe the interactions between ions and electrons.[31] With convergence testing, the plane-wave cutoff energy of 400 eV and k-point meshes of $3 \times 2 \times 3$ were used to ensure the accuracy and efficiency of calculations. The threshold for self-consistent field iterations was 5.0×10^{-7} eV per atom. The convergence tolerance parameters of optimized calculation were the energy of 1.0×10^{-5} eV per atom, the maximum force of 0.03 eV Å^{-1}, the maximum inner stress of 0.05 GPa and the maximum displacement of 1.0×10^{-4} nm. After finishing geometry optimizations, electronic, optical and mechanical properties of all models were calculated. The lattice stabilities of all the optimized structures were evaluated by the phonon dispersions, where the imaginary frequency was the sign of lattice instability.[32,33]

Considering no experimental report of the preparation of pure $SrSi_6N_8O$, we used the acid–base idea as mentioned by M. Mikami[34] to assume the solid-state reaction for production of $SrSi_6N_8O$. The binary oxide is generally considered as acid while binary nitride as base. So the reaction for production of $SrSi_6N_8O$ should be defined as following:

$$SrO + 2Si_3N_4 \rightarrow SrSi_6N_8O \qquad (1)$$

The formation energy (E_{form}) of reaction [1] was calculated as following equation:

$$E_{form} = E_{SrSi_6N_8O} - E_{SrO} - 2E_{Si_3N_4} \qquad (1)$$

where the $E_{SrSi_6N_8O}$, E_{SrO} and $E_{Si_3N_4}$ were the total energies of $SrSi_6N_8O$, SrO and α-Si_3N_4, respectively. A negative value of formation energy indicates the reaction is exothermic and the production is stable.

The binding energy (E_b) can be used to investigate the relative stability of the model. The value of binding energies of all models were calculated by the following formula:[35]

$$E_b = \frac{E_{tot} - (n_{Si}\mu_{Si} + n_N\mu_N + n_O\mu_O)}{n_{Si} + n_N + n_O} \qquad (2)$$

where the E_{tot} was the total energy of the considered model, and the chemical potentials of Si, N and O were defined as $\mu_{Si} = \mu_{bulk-Si}$, $\mu_N = \mu_{N_2}/2$ and $\mu_O = \mu_{O_2}/2$, respectively.[36,37] The coefficients n_{Si}, n_N and n_O were the numbers of the Si, N and O atoms in each model. For O-doped $SrSi_6N_8$ models, the values of bonding energies were used to predict the preferential position for O doping in the lattice of $SrSi_6N_8$.

Understanding elastic properties of nitridosilicates is very important for their application and improvement. For

orthorhombic crystals, it is known that the mechanical stability requires elastic constants satisfying the following conditions:[38,39]

$$c_{ij} > 0 \ (i = 1 \sim 6),$$

$$c_{11} + c_{22} + c_{33} + 2c_{12} + 2c_{13} + 2c_{23} > 0,$$

$$c_{11} + c_{22} - 2c_{12} > 0,$$

$$c_{11} + c_{33} - 2c_{13} > 0,$$

$$c_{22} + c_{33} - 2c_{23} > 0 \qquad (3)$$

The mechanical constants: bulk modulus (B), shear modulus (G), Young's modulus (E), and Poisson's ratio (v) have been calculated using the following equations:[38,39]

$$B = (1/9)(c_{11} + c_{22} + c_{33} + 2c_{12} + 2c_{13} + 2c_{23}) \qquad (4)$$

$$G = (1/15)[(c_{11} + c_{22} + c_{33} + 3(c_{44} + c_{55} + c_{66}) - c_{12} - c_{13} - c_{23})] \qquad (5)$$

$$E = 9BG/(3B + G) \qquad (6)$$

$$v = (1/2)(3B - 2G)/(3B + G) \qquad (7)$$

3. Results and discussion

3.1 Geometry optimization results

Table 1 lists the calculated lattice parameters, average bond lengths and binding energies of all models. The lattice parameters of $2 \times 2 \times 1$ $SrSi_6N_8$ and $2 \times 2 \times 1$ $SrSi_6N_8O$ supercells are well agreement with previous results.[9,24] There is no big change in the lattice parameters after O doping into $SrSi_6N_8$. The slight volume expansions come from the changes of local bond lengths. The average bond lengths of Si–O[2] and Si–O[3] are larger than the Si–N[2] and Si–N[3] in O_i–$SrSi_6N_8$ ($i = 1$, 2 and 3), while the average bond length of Si–O[2] is smaller than the Si–N[2] in O_4–$SrSi_6N_8$. The results indicate that different coordination environments of O atom has different effects on the

Si–O bond lengths. The E_{form} of pure $SrSi_6N_8O$ calculated by eqn (1) is -0.37 eV, which indicates that the reaction [1] is somewhat exothermic and $SrSi_6N_8O$ is stable. The lower value of E_b indicates the more stable degree of the model. The E_b (-1.71 eV) of $SrSi_6N_8O$ means that it has the more stable crystal structure and can be easier to synthesis compared with $SrSi_6N_8$ (-1.40 eV). These phenomenon is corresponding to the fact that $SrSi_6N_8$ is a kind of reduced nitridosilicate and must be synthesized under the condition of extreme lack of oxygen.[9] The E_b of O_4–$SrSi_6N_8$ (-1.45 eV) is the lowest one among all O-doped $SrSi_6N_8$ models, meaning that O atom prefers to insert into the single Si–Si bond to stabilize the crystal structure of $SrSi_6N_8$.

Furthermore, phonon dispersions of all optimized models have been calculated to evaluate the structural stability, as seen in Fig. 2. The results shows that there is no imaginary frequency of pure $SrSi_6N_8$ and $SrSi_6N_8O$, which means that $SrSi_6N_8$ and $SrSi_6N_8O$ are structurally stable. The lowest frequencies of O_i–$SrSi_6N_8$ ($i = 1$, 2, 3 and 4) are -0.20, -0.81, -0.53 and -0.05 THz, respectively. According to the previous works, the small negative frequencies of O_1–$SrSi_6N_8$ and O_4–$SrSi_6N_8$ could be ignored because the small negative frequencies may be caused by the relatively smaller supercells and lower computational accuracies.[32,33] However, the calculation of phonon dispersion is time consuming with a bigger supercell and higher computational accuracy. So we think it is reasonable to consider O_1–$SrSi_6N_8$ and O_4–$SrSi_6N_8$ as structurally stable models based on the calculated phonon dispersions. While, the structures of O_2–$SrSi_6N_8$ and O_3–$SrSi_6N_8$ are metastable or unstable according to their obvious imaginary frequencies as seen in Fig. 2(d) and (e). The results of phonon dispersions are well agreement with the results of bonding energies (E_b), which means that the structures of O_1–$SrSi_6N_8$ and O_4–$SrSi_6N_8$ are more stable than O_2–$SrSi_6N_8$ and O_3–$SrSi_6N_8$.

3.2 Electronic properties

Fig. 3 shows the band structures and partial density of states (PDOS) of $SrSi_6N_8$ and $SrSi_6N_8O$. The calculated bandgaps (E_g) of $SrSi_6N_8$ and $SrSi_6N_8O$ are 3.10 and 3.97 eV, respectively. Although, there is no experimentally reported the E_g of $SrSi_6N_8$

Table 1 Optimized lattice parameters, bond lengths and binding energies of all models

	Lattice parameters (Å)				Average bond length (Å)					
Models	a	b	c	Volume (Å³)	Si–N[2]	Si–N[3]	Si–Si	Si–O[2]	Si–O[3]	E_b (eV)
$SrSi_6N_8$	9.664	15.854	9.331	1429.56	1.679	1.755	2.379			-1.40
$SrSi_6N_8$[a]	4.801	7.855	9.260	349.21			2.352			
$SrSi_6N_8$[b]	4.803	7.836	9.261	350.93						
O_1–$SrSi_6N_8$	9.682	15.897	9.302	1431.80	1.680	1.757	2.367	1.688		-1.43
O_2–$SrSi_6N_8$	9.679	15.869	9.331	1433.13	1.678	1.757	2.370		1.850	-1.42
O_3–$SrSi_6N_8$	9.670	15.890	9.320	1432.10	1.679	1.757	2.370		1.811	-1.42
O_4–$SrSi_6N_8$	9.673	15.939	9.400	1449.29	1.681	1.756	2.406	1.589		-1.45
$SrSi_6N_8O$	9.722	16.400	9.706	1547.62	1.683	1.752		1.620		-1.71
$SrSi_6N_8O$[a]	4.865	8.206	9.721							

[a] Ref. 9. [b] Ref. 19.
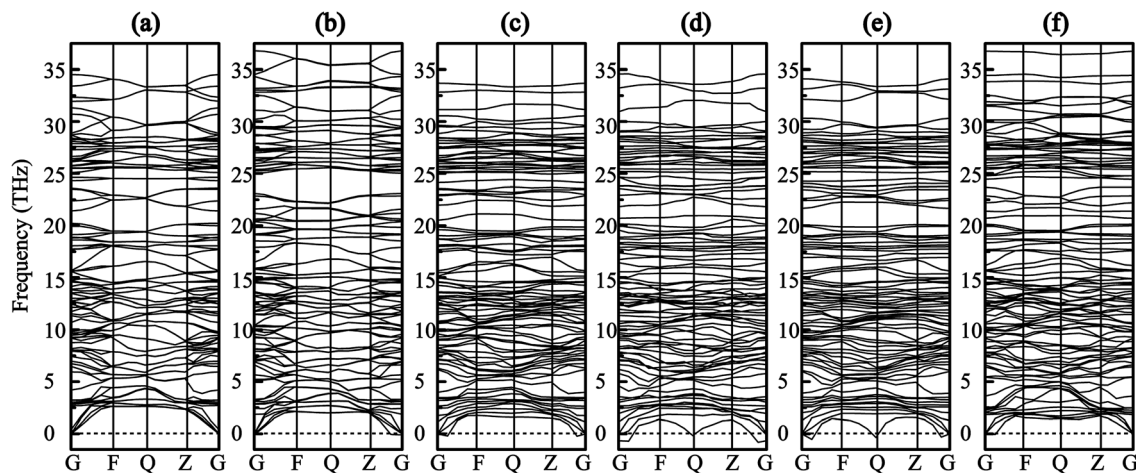
Fig. 2 Phonon dispersion curves (a) $SrSi_6N_8$, (b) $SrSi_6N_8O$, (c) $O_1–SrSi_6N_8$, (d) $O_2–SrSi_6N_8$, (e) $O_3–SrSi_6N_8$ and (f) $O_4–SrSi_6N_8$.

or $SrSi_6N_8O$, our GGA calculated E_g are expected to be smaller than experimental values since the underestimation of GGA calculation.[39] While the effects of oxygen on electronic

Fig. 3 Band structures and partial density of states (PDOS) of (a) $SrSi_6N_8$ and (b) $SrSi_6N_8O$.

properties of $SrSi_6N_8$ can be expounded through the relative changes. The top of valence bands of $SrSi_6N_8$ and $SrSi_6N_8O$ are occupied by N 2p states. Differing in band structures from the other alkaline-earth-metal nitridosilicates,[6] there are some energy levels below the conduction bands of $SrSi_6N_8$, which are mainly constituted of Si 3p states as seen from the PDOS. Furthermore, the 3p states of Si_1 contribute the more parts of the bottom of conduction bands compared to Si_2, which indicates that the energy levels below the conduction bands are attributed to the single Si–Si bond. The previous works reported that Si–Si bond forms an empty σ* state under the bottom of conduction bands in some nitrides.[40,41] Therefore, the Si–Si σ* state is the main reason for the lower bandgap of $SrSi_6N_8$ compared to $SrSi_6N_8O$.

Furthermore, the electron density distribution (EDD) plots are calculated to investigate the difference between Si–Si and Si–O–Si bonds. Fig. 4(a) and (b) illustrate the partial atom distributions and corresponding EDD plots on the (010) plane of $SrSi_6N_8$ and $SrSi_6N_8O$, respectively. We can find that there is
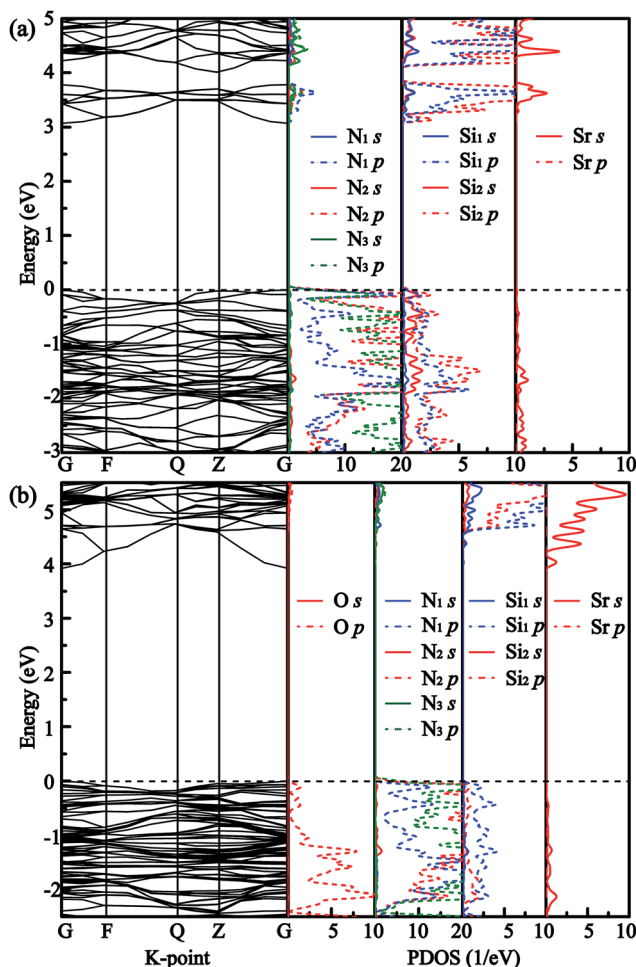

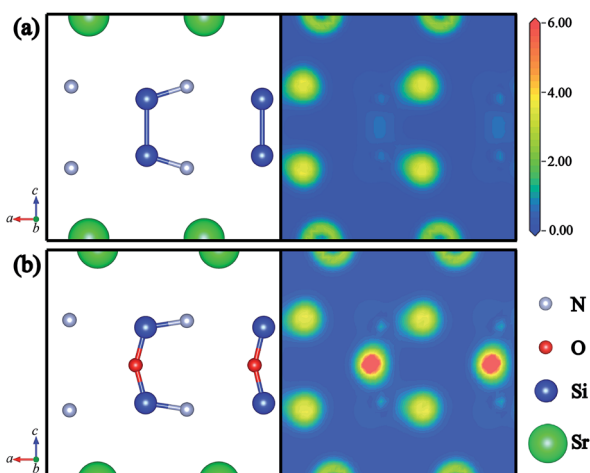**Fig. 4** Partial atom distributions and corresponding electron density distribution plots of (a) $SrSi_6N_8$ and (b) $SrSi_6N_8O$ on the (010) plane.

a small amount of electron density distributing in the center of Si–Si bond in $SrSi_6N_8$, while a high density of electron gathers on the O atoms in $SrSi_6N_8O$. The stronger electronic interaction of Si–O–Si bond gives the more stable crystal structure for $SrSi_6N_8O$, which is consistent with results of the calculated E_b. Besides, the electron densities of O atoms are obviously higher than that of N atoms in $SrSi_6N_8O$, which is attributed to the stronger electronegativity of O atom.

The calculated band structures and PDOS of the O atoms and its adjacent Si atoms for all O-doped $SrSi_6N_8$ models are plotted in Fig. 5. The calculated bandgaps (E_g) of O_i–$SrSi_6N_8$ ($i = 1, 2, 3$ and 4) are 3.17, 2.84, 3.09 and 3.33 eV, respectively. For O_1–$SrSi_6N_8$, as seen in Fig. 5(a), the band structure of O_1–$SrSi_6N_8$ is very close to that of undoped $SrSi_6N_8$, which indicates that the $O^{[2]}$ has the similar properties of $N^{[2]}$. As seen in Fig. 5(b) and (c), the reason of the E_g decreasing for O_2–$SrSi_6N_8$ and O_3–$SrSi_6N_8$ is that the hybrid Si–O bonds generate energy levels under the conduction bands. For O_4–$SrSi_6N_8$, the distribution of O 2p states are very similar to that of $SrSi_6N_8O$, showing that the O_4 atom has the same character to the O atoms in $SrSi_6N_8O$. The E_g of O_4–$SrSi_6N_8$ is larger than that of $SrSi_6N_8$, which indicates that inserting O atom into the single Si–Si bond to decrease the concentration of Si–Si bonds can increase the E_g.

3.3 Optical properties

The absorption coefficient is one of key parameters to evaluate the performance for phosphors. The absorption spectra can be described in terms of time-dependent perturbations of the ground-state electronic states, which has always been investigated combined the electron transition between valance bonds
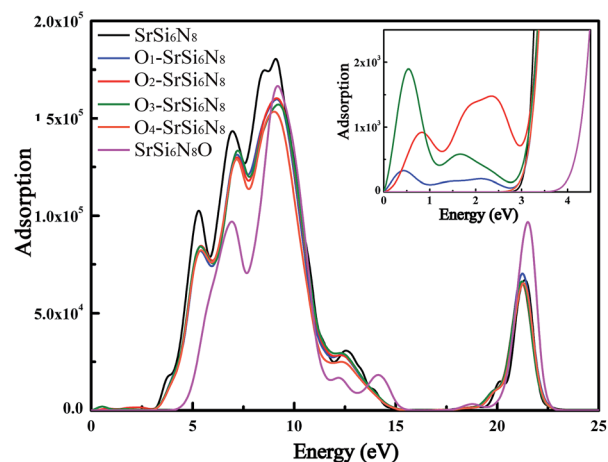

Fig. 6 Calculated absorption spectra of $SrSi_6N_8$, $SrSi_6N_8O$ and O-doped $SrSi_6N_8$ models.

and conduction bonds.[42] Fig. 6 shows the calculated absorption spectra of all models. The absorption peak for undoped $SrSi_6N_8$ is located at about 3.0–15.0 eV, which are corresponding to the electron transitions from N 2p states in the valence bands to Si 3p and Sr 5s states in the conduction bands as shown from PDOS in Fig. 3(a). The absorption edge of $SrSi_6N_8O$ starts at 3.9 eV, with a large blue shift compared to that of $SrSi_6N_8$ at 2.9 eV. The positions of the main absorption peaks for O_i–$SrSi_6N_8$ ($i = 1, 2, 3$ and 4) are almost the same as $SrSi_6N_8$, while the absorption intensities become lower. Besides, as show in the enlarged view in Fig. 5, the weak peaks located around 0–3.0 eV of the O_2–$SrSi_6N_8$ and O_3–$SrSi_6N_8$ derive from the electron
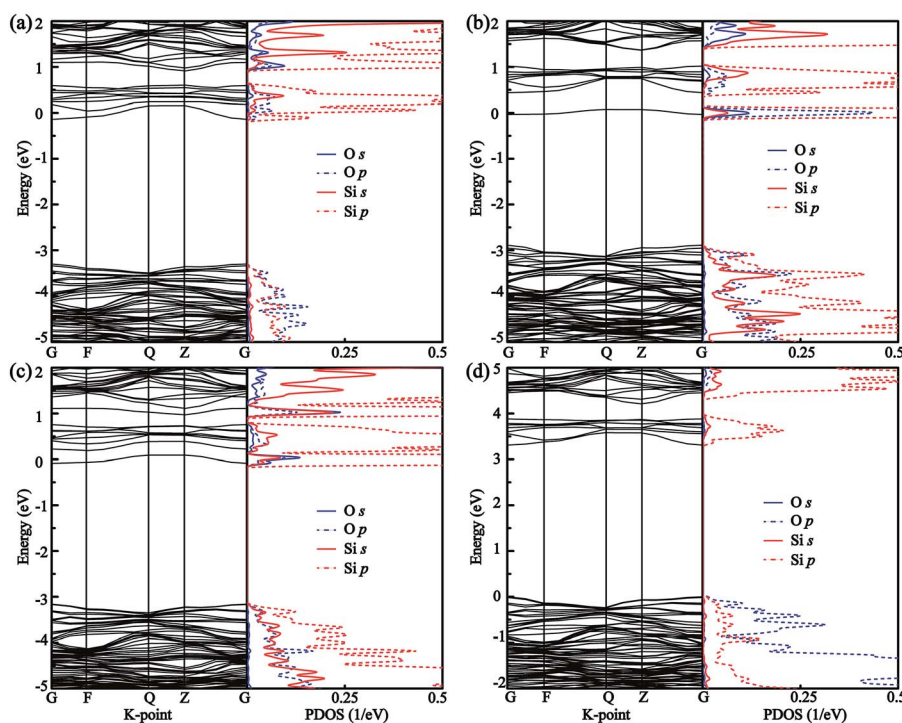
Fig. 5 Band structures and PDOS of (a) O_1–$SrSi_6N_8$, (b) O_2–$SrSi_6N_8$, (c) O_3–$SrSi_6N_8$, and (d) O_4–$SrSi_6N_8$.
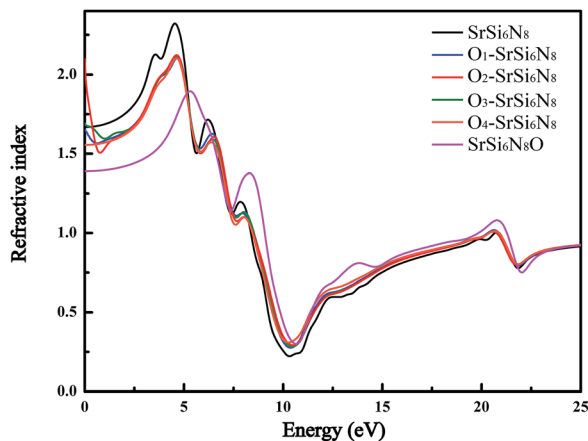
Fig. 7 Calculated refractive spectra of $SrSi_6N_8$, $SrSi_6N_8O$ and O-doped $SrSi_6N_8$ models.

transitions between Si–O hybrid states under the bottom of conduction bands and conduction bands, as shown in Fig. 5(b) and (c).

Fig. 7 shows the refractive spectra of $SrSi_6N_8$, $SrSi_6N_8O$ and O-doped $SrSi_6N_8$ models. Although, there is no experimentally reported refractive index (n) of $SrSi_6N_8$ or $SrSi_6N_8O$, the static refractive indexes (n_0) of $SrSi_6N_8$ (1.67) and $SrSi_6N_8O$ (1.39) are expected to be lower than the experimental value due to the underestimated calculation of GGA-PEB.[39] Nevertheless, the relative changes can reflect the effects of O atoms on $SrSi_6N_8$. The calculated static refractive indexes of O_i–$SrSi_6N_8$ ($i = 1, 2$ and 3 and 4) are 1.65, 2.08, 1.69 and 1.56, respectively, which are well corresponding to Moss rule that the static refractive index is inversely proportional to the E_g.[43] Except for the static refractive indexes, the main peaks of refractive indexes of all O-doped $SrSi_6N_8$ models are lower than that of $SrSi_6N_8$. Furthermore, compared with $SrSi_6N_8$, the locations of main peaks for $SrSi_6N_8O$ are significantly blue-shift. The results of optical properties show that different doping sites of O atoms in $SrSi_6N_8$ have different effects on its basic absorption and refractive spectra.

3.4 Mechanical properties

The optimized structures of all models have been applied to calculate the elastic tensors which consist of nine independent components, as tabulated in Table 2. It can be seen that the relationships of elastic constants satisfy the conditions as shown in eqn (3), which indicates that $SrSi_6N_8$, $SrSi_6N_8O$ and O-doped $SrSi_6N_8$ are mechanically stable.

Table 3 Calculated bulk modulus B (GPa), shear modulus G (GPa), Young's modulus E (GPa) and Poisson's ratio v for all models

Models	B	G	E	v
$SrSi_6N_8$	175.92	111.84	276.85	0.24
O_1–$SrSi_6N_8$	150.5	102.58	250.77	0.22
O_2–$SrSi_6N_8$	174.99	116.7	286.43	0.23
O_3–$SrSi_6N_8$	174.33	112.15	277.04	0.24
O_4–$SrSi_6N_8$	170.93	100.6	252.30	0.25
$SrSi_6N_8O$	181.09	113.85	282.37	0.24

Furthermore, the mechanical constants: bulk modulus (B), shear modulus (G), Young's modulus (E), and Poisson's ratio (v) for all models are listed in Table 3. The mechanical constants: B, G and E of $SrSi_6N_8O$ are larger than that of $SrSi_6N_8$, which mainly attributes to the more stable Si–O–Si bond than Si–Si bond. Though introducing O atom produces a certain degree of lattice distortion in $SrSi_6N_8$, there is no obvious deterioration on mechanical properties of O-doped $SrSi_6N_8$ compared to undoped $SrSi_6N_8$, even some mechanical constants are improved. Besides, with the comparison of traditionally mechanical ceramics such as sialons ($B = 170$–240 GPa, $G = 118.84$ GPa and $E = 197$–283 GPa),[44,45] the mechanical properties of all models considered in this work indicate that they have the application prospect for mechanical ceramics.

4. Conclusions

In this work, first-principles simulation has been performed to investigate the structural, electronic, optical and mechanical properties of $SrSi_6N_8$, $SrSi_6N_8O$ and O-doped $SrSi_6N_8$. Firstly, this work has given the comparison and explanation of the difference between the two structurally similar nitridosilicates $SrSi_6N_8$ and $SrSi_6N_8O$. The results show that $SrSi_6N_8O$ is more stable than $SrSi_6N_8$, and the E_g of $SrSi_6N_8O$ is larger than that of $SrSi_6N_8$. The key factor of the difference between $SrSi_6N_8$ and $SrSi_6N_8O$ is the O atom. Namely, the Si–O–Si bond is stronger than the single Si–Si bond, which contributes to the more stable crystal structure of $SrSi_6N_8O$. And the Si–Si σ* states under the conduction bonds are the main reason for the smaller E_g of $SrSi_6N_8$ compared to $SrSi_6N_8O$.

Secondly, the effects of O on electronic, optical and mechanical properties of $SrSi_6N_8$ have been investigated systematically. The crystal structure of $SrSi_6N_8$ can be stabilized with doping O into the lattice and the most preferential doping position of O is

Table 2 Calculated elastic tensor C_{ij} (GPa) for all models

Models	C_{11}	C_{22}	C_{33}	C_{44}	C_{55}	C_{66}	C_{12}	C_{13}	C_{23}
$SrSi_6N_8$	380.08	308.27	341.91	94.79	81.51	131.64	91.21	84.21	101.08
O_1–$SrSi_6N_8$	272.6	288.96	349.77	76.14	120.84	85.98	88.23	68.13	65.22
O_2–$SrSi_6N_8$	326.66	320.01	376.75	89.42	148.04	96.83	102.69	95.72	77.35
O_3–$SrSi_6N_8$	308.17	332.72	378.19	83.16	133.37	96.20	100.24	94.78	79.93
O_4–$SrSi_6N_8$	299.77	320.38	371.85	81.32	135.48	96.61	99.14	96.71	77.35
$SrSi_6N_8O$	324.25	377.85	374.25	92.30	67.54	142.86	85.77	71.16	119.8

insertion between the single Si–Si bonds. And introducing O into the Si–Si bond can significantly increase the E_g of $SrSi_6N_8$. The static refractive indexes become larger for O substituting to N models while become smaller for the O insert into the Si–Si bond. Besides, the calculated mechanical constants are comparable to traditionally mechanical ceramics such as sialons, which indicates $SrSi_6N_8$, $SrSi_6N_8O$ and O-doped $SrSi_6N_8$ have potential applications as mechanical materials. This work is helpful to understand the difference between $SrSi_6N_8$ and $SrSi_6N_8O$, and opens up their possibility of new application.

Acknowledgements

Notes and references

1 R. J. Xie and N. Hirosaki, *Sci. Technol. Adv. Mater.*, 2007, **8**, 588–600.

2 S. Ye, F. Xiao, Y. X. Pan, Y. Y. Ma and Q. Y. Zhang, *Mater. Sci. Eng., R*, 2010, **71**, 1–34.

3 M. Zeuner, S. Pagano and W. Schnick, *Angew. Chem., Int. Ed.*, 2011, **50**, 7754–7775.

4 N. Lakshminarasimhan and U. V. Varadaraju, *J. Electrochem. Soc.*, 2005, **152**, H152–H156.

5 S. M. Jacobsen, *J. Soc. Inf. Disp.*, 1996, **4**, 331–335.

6 R. J. Xie, Y. Q. Li, N. Hirosaki and H. Yamamoto, *Nitride Phosphors and Solid-State Lighting*, Taylor & Francis, 2011.

7 P. Schmidt, A. Tuecks, J. Meyer, H. Bechtel, D. Wiechert, R. Mueller-Mach, G. Mueller and W. Schnick, *7th Inter. Conf. Solid State Lighting*, 2007.

8 H. Huppertz and W. Schnick, *Z. Anorg. Allg. Chem.*, 1997, **623**, 212.

9 F. Stadler, O. Oeckler, J. Senker, H. A. Höppe, P. Kroll and W. Schnick, *Angew. Chem., Int. Ed.*, 2005, **117**, 573–576.

10 F. Stadler and W. Schnick, *Z. Anorg. Allg. Chem.*, 2007, **633**, 589–592.

11 G. Pilet, H. A. Höppe, W. Schnick and S. Esmaeilzadeh, *Solid State Sci.*, 2005, **7**, 391.

12 Y. Q. Li, A. C. A. Delsing, R. Metslaara, G. de Witha and H. T. Hintzen, *J. Alloys Compd.*, 2009, **487**, 28.

13 M. Zeuner, F. Hintze and W. Schnick, *Chem. Mater.*, 2009, **21**, 336.

14 K. S. Sohn, B. Lee, R. J. Xie and N. Hirosaki, *Opt. Lett.*, 2009, **34**, 3427.

15 H. Nersisyan, H. I. Won and C. W. Won, *Chem. Commun.*, 2011, **47**, 11897.

16 C. J. Duan, X. J. Wang, W. M. Otten, A. C. A. Delsing, J. T. Zhao and H. T. Hintzen, *Chem. Mater.*, 2008, **20**, 1597.

17 H. Yamane and F. J. DiSalvo, *J. Alloys Compd.*, 1996, **240**, 33–36.

18 K. Shioi, N. Hirosaki, R. J. Xie, T. Takeda and Y. Li, *J. Mater. Sci.*, 2008, **43**, 5659–5661.

19 S. M. Wu, H. E. Hung, C. H. Hsieh, Y. C. Lin, L. C. Wang, Y. T. Tsai, C. C. Lin and R. S. Liu, *J. Am. Ceram. Soc.*, 2015, **98**, 2662–2669.

20 Z. Shen, J. Grins, S. Esmaeilzadeh and H. Ehrenberg, *J. Mater. Chem.*, 1999, **9**, 1019–1022.

21 N. Karkada, D. Porob, N. K. Prasanth and A. Setlur, *ECS Trans.*, 2009, **16**, 41–50.

22 R. J. Xie, N. Hirosaki, Y. Li and T. Takeda, *J. Lumin.*, 2010, **130**, 266–269.

23 S. A. Fartode, B. S. Reddy, V. Nayar and S. J. Dhoble, *Ferroelectr., Lett. Sect.*, 2016, **43**, 34–51.

24 Y. H. Song, T. Y. Choi, Y. Y. Luo, K. Senthil and D. H. Yoon, *Opt. Mater.*, 2011, **33**, 989–991.

25 Z. Wang, B. Shen, F. Dong, S. Wang and W. S. Su, *Phys. Chem. Chem. Phys.*, 2015, **17**, 15065–15070.

26 C. W. Yeh, Y. P. Liu, Z. R. Xiao, Y. K. Wang, S. F. Hu and R. S. Liu, *J. Mater. Chem.*, 2012, **22**, 5828–5834.

27 G. Kresse and D. Joubert, *Phys. Rev. B: Condens. Matter Mater. Phys.*, 1999, **59**, 1758.

28 Q. Peng, X. J. Chen, S. Liu and S. De, *RSC Adv.*, 2013, **3**, 7083–7092.

29 M. D. Segall, P. J. Lindan, M. A. Probert, C. J. Pickard, P. J. Hasnip, S. J. Clark and M. C. Payne, *J. Phys.: Condens. Matter*, 2002, **14**, 2717.

30 J. P. Perdew, K. Burke and M. Ernzerhof, *Phys. Rev. Lett.*, 1996, **77**, 3865.

31 M. Marlo and V. Milman, *Phys. Rev. B: Condens. Matter Mater. Phys.*, 2000, **62**, 2899.

32 L. Zhu, L. Li, T. Cheng and D. Xu, *J. Mater. Chem. A*, 2015, **3**, 5449–5456.

33 S. S. Bhat, U. V. Waghmare and U. Ramamurty, *Cryst. Growth Des.*, 2014, **14**, 3131–3141.

34 M. Mikami, *ECS J. Solid State Sci. Technol.*, 2013, **2**, R3048–R3058.

35 S. Yang, D. Li, T. Zhang, Z. Tao and J. Chen, *J. Phys. Chem. C*, 2011, **116**, 1307–1312.

36 F. Oba, K. Tatsumi, I. Tanaka and H. Adachi, *J. Am. Ceram. Soc.*, 2002, **85**, 97–100.

37 K. Yang, Y. Dai and B. Huang, *J. Phys. Chem. C*, 2007, **111**, 12086–12090.

38 Z. Wu, X. Hao, X. Liu and J. Meng, *Phys. Rev. B: Condens. Matter Mater. Phys.*, 2007, **75**, 054115.

39 B. Tu, H. Wang, X. Liu, W. Wang and Z. Fu, *J. Am. Ceram. Soc.*, 2014, **97**, 2996–3003.

40 L. E. Hintzsche, C. M. Fang, M. Marsman, G. Jordan, M. W. P. E. Lamers, A. W. Weeber and G. Kresse, *Phys. Rev. B: Condens. Matter Mater. Phys.*, 2013, **88**, 155204.

41 Z. Huang, F. Chen, Q. Shen and L. Zhang, *RSC Adv.*, 2016, **6**, 7568–7574.

42 R. Asahi, Y. Taga, W. Mannstadt and A. J. Freeman, *Phys. Rev. B: Condens. Matter Mater. Phys.*, 2000, **61**, 7459.

43 T. S. Moss, *Phys. Status Solidi B*, 1985, **131**, 415–427.

44 J. Hafner, Z. Lenčéš and P. Šajgalík, *J. Am. Ceram. Soc.*, 2003, **86**, 1162–1167.

45 L. Benco, J. Hafner, Z. Lences and P. Sajgalik, *J. Eur. Ceram. Soc.*, 2008, **28**, 995–1002.